# Irradiation resistance properties studies on helium ions irradiated MAX phase $Ti_3AlC_2$

Peng Song [a,b], Jianrong Sun [a,*], Zhiguang Wang [a,*], Minghuan Cui [a], Tielong Shen [a], Yuanfei Li [a], Lilong Pang [a], Yabin Zhu [a], Qing Huang [c], Jinjun Lü [d]

[a] Institute of Modern Physics, Chinese Academy of Sciences, Lanzhou 730000, China
[b] University of Chinese Academy of Sciences, Beijing 100049, China
[c] Ningbo Institute of Materials Technology & Engineering, Chinese Academy of Sciences, Ningbo 315201, China
[d] Lanzhou Institute of Chemical Physics, Chinese Academy of Sciences, Lanzhou 730000, China



ARTICLE INFO

*Keywords:*
He
MAX phase
Irradiation resistance
$Ti_3AlC_2$

ABSTRACT

The study presents an investigation of irradiation resistance properties of $Ti_3AlC_2$ under 500 keV He ions irradiation with the doses ranging from $5.0 \times 10^{16}$ to $1.0 \times 10^{18}$ ions $cm^{-2}$ at certain temperatures, like room temperature (RT), 300 and 500 °C. X-ray diffraction (XRD) and Transmission electron microscopy (TEM) are used to study the evolution of structural damage and the behavior of deposited He ions respectively. XRD analysis reveals that for the highest dose irradiation (~52 dpa at peak), no amorphization occurs. And the structural recovery of $Ti_3AlC_2$ is more significant accompanied with the gradual disappearance of the irradiation-induced TiC phase as the temperature rises from RT to 300 and to 500 °C with the same dose irradiation. TEM observations show that He bubbles appear in the shapes of sphere, string and platelet but no big bubbles are formed for all irradiations. Moreover, no large cracks form in the sample implanted with the highest helium concentration of $\sim 6.4 \times 10^5$ appm.

## 1. Introduction

As one of the typical MAX phases, where M is an early transition metal, A is an element from the IIIA or IVA groups, and X is carbon or nitrogen, $Ti_3AlC_2$ is characterized by near close-packed Ti layers interleaved with Al layers, with the C atoms filling the octahedral sites between Ti atoms ($Ti_6C$) [1]. So $Ti_3AlC_2$ combines the properties of both metal and ceramic, such as high-temperature stability (1460 °C at least), good ductility, excellent thermal shock resistance and intrinsic damage tolerance [1–4]. Therefore, it has been considered as a remarkable fuel cladding or structural material to be used in future fission and fusion reactors, such as the gas-cooled fast reactor (GFR) and international thermonuclear experimental reactor (ITER).

Several works concerning irradiation effect of $Ti_3AlC_2$ and similar MAX phase $Ti_3SiC_2$ have been conducted in recent years and most of them are at low damage displacement with high energy ions irradiation. Flem et al. [5] and Whittle et al. [6] confirmed that $Ti_3$ (Si, Al) $C_2$ remained crystalline at 6.67 and ~25 dpa respectively except for some loss of its nanolamellar structure. It was also shown by Whittle group that $Ti_3AlC_2$ showed more tolerance to irradiation damage than $Ti_3SiC_2$. Liu et al. [7,8] have demonstrated an evident increase in hardness and the formation of β-$Ti_3Si_{0.90}Al_{0.10}C_2$ after irradiation by 74 MeV Kr and 92 MeV Xe ions as well as a complete recovery of properties at high temperature especially at 800 °C. However, the researches regarding the helium effect on $Ti_3AlC_2$ are rare though in (n, α) transmutation reactions [9] of nuclear materials plenty of helium atoms are produced, which result in deleterious effects such as swelling, blistering and mechanical properties degradation of materials [10]. Wang et al. [11] found the transformation of He bubbles shape from sphere to string in $Ti_3AlC_2$ with 50 keV He irradiation at room temperature. But there is no work studying the He behaviors in $Ti_3AlC_2$ at high irradiation temperature. This work is carried out to develop an understanding of the irradiation resistance of $Ti_3AlC_2$ and the evolution of helium bubbles under different He ions irradiation conditions.

## 2. Experimental details

The polycrystalline $Ti_3AlC_2$ was provided by Ningbo Institute of Materials Technology & Engineering, Chinese Academy of Sciences. To obtain the material, a mixture powder of Ti, Al and C with the stoichiometric proportion of 3:1.2:1.9 should be put into a cylindrical graphite mould with 5 min sintering at 1200 °C in the flowing argon gas with an applied pressure of 30 MPa by the spark plasma sintering technique. The specimens were cut into parallelepipeds of about $10 \times 10 \times 2$ $mm^3$, and one face was polished with diamond spray of particle size down to 1 μm. The parallelepipeds

* Corresponding authors. Tel.: +86 9314969647.
*E-mail addresses:* sunjr@impcas.ac.cn (J. Sun), zhgwang@impcas.ac.cn (Z. Wang).

were cleaned by rinsing in ultrasonic baths of acetone and ethanol and subsequently irradiated on the polished surface.

Irradiation experiments of the $Ti_3AlC_2$ ceramic were performed at 320 keV multi-discipline research platform for highly charged ions equipped with an ECR (electron cyclotron resonance) ion source in the Institute of Modern Physics, Chinese Academy of Sciences (IMP, CAS), Lanzhou. The samples are irradiated with 500 keV $He^{2+}$ ions and the mean flux was about 5 μA ($1.1 \times 10^{13}$ ions $cm^{-2}$ $s^{-1}$). The irradiation conditions are summarized in Table 1. The theoretical results of 500 keV He irradiation with a dose of $1.0 \times 10^{18}$ ions $cm^{-2}$, i.e. penetration depth, displacement damage (dpa, displacement per atom) and He concentration are calculated by SRIM 2008 [12] full damage cascade simulations (Fig. 1). The threshold displacement energies are determined as 25 eV for Ti, 25 eV for Al and 28 eV for C.

All samples were characterized by low-incidence X-ray diffraction (LI-XRD) using a Philips X'pert diffractometer with Cu Kα radiation. The X-ray diffraction data were collected between 20° and 85° in 2θ scale under an incidence of 5° with the corresponding maximum depth of about 1.5 μm. The data from the irradiated zone was covered in XRD data according to the SRIM calculation results. The irradiated specimens are prepared by the cross-sectional specimen technique and then thinned by 3.0 keV Ar+ ion beam milling to form a wedge for sufficient electronic transparency, so that damage level as a function of depth could be obtained directly. The TEM observation is performed with an FEI TECNAI $G^2$ F30 and all micrographs are taken at 300 keV.

## 3. Results

### 3.1. XRD patterns

XRD diffraction patterns of the virgin sample and all irradiated samples are shown in Fig. 2. With increasing doses of samples irradiated at RT, an evident drop of peak intensity and rise of peak width are found, which reveals some loss of crystallinity. Both (102) and (112) peaks begin to shift remarkably to higher 2θ and (105) peak to lower 2θ with the similar trend when the irradiation dose reaches $5.0 \times 10^{16}$ ions $cm^{-2}$. This phenomenon is principally caused by the presence of new TiC phase whose corresponding peaks are (111), (200) and (220). It has been previously confirmed that the TiC phase is produced by nuclear shock in irradiated $Ti_3SiC_2$ or $Ti_3AlC_2$ [11,13–15]. In addition, the relative intensities of (102) and (103) to (101) peaks become larger as the irradiation dose increases. It might be induced by the phase transformer from α-$Ti_3AlC_2$ to β-$Ti_3AlC_2$ and the similar transformation has been found in $Ti_3SiC_2$ after irradiation [8,14]. Furthermore, Farber et al. have verified these polymorphic phase transformations in $Ti_{n+1}AX_n$ ($n \geqslant 2$), such as $Ti_3SiC_2$, $Ti_3AlC_2$ and $Ti_4AlN_3$ through HRTEM [16].

For the samples irradiated with the dose of $3.0 \times 10^{17}$ ions $cm^{-2}$ at various temperatures, the peak intensity, peak position and peak width recovered progressively as the irradiation temperature increased. That phenomenon serves as proof of the beneficial effect of temperature in reducing irradiation damage. Moreover, the new phases formed with irradiation at RT cannot be detected when the irradiation temperature increases to 500 °C. Considering the noteworthy thermal stability of the new phase TiC up to 820 °C [14], we conclude that the possibility of TiC formation is eliminated by the recombination of irradiation effects during collision cascade formation.

**Table 1**
The parameters of irradiation experimental condition.

| Temperature | Room temperature | 300 °C | 500 °C |
|---|---|---|---|
| Irradiation dose (ions $cm^{-2}$) | $5.0 \times 10^{16}$<br>$1.0 \times 10^{17}$<br>$3.0 \times 10^{17}$<br>$1.0 \times 10^{18}$ | $3.0 \times 10^{17}$ | $3.0 \times 10^{17}$ |

### 3.2. TEM results

The TEM analysis confirmed the presence of polycrystalline $Ti_3AlC_2$ with a grain size of ~1.5 μm (not shown). And an overview of the nanolamellar structure and damage area is shown in Fig. 3. In the virgin sample, the periodic multilayer structures are evident (Fig. 3a). With the irradiation dose of $5.0 \times 10^{16}$ ions $cm^{-2}$ (~2.62 dpa), it is detected obviously that the depth of the damaged area ranges from 1.134 to 1.354 μm in accordance with the SRIM calculation results. And some isolated nanometer-scale spherical helium bubbles are spread at the damaged region with an average radius of ~0.6 nm around the maximum concentration ($3.2 \times 10^4$ appm) depth of implanted He atoms (Fig. 3b). The bubble radius presents a Gaussian-like distribution and the mean radius is determined by measuring the radius of a total of 80 bubbles [11]. In addition, the damaged area contains clusters of

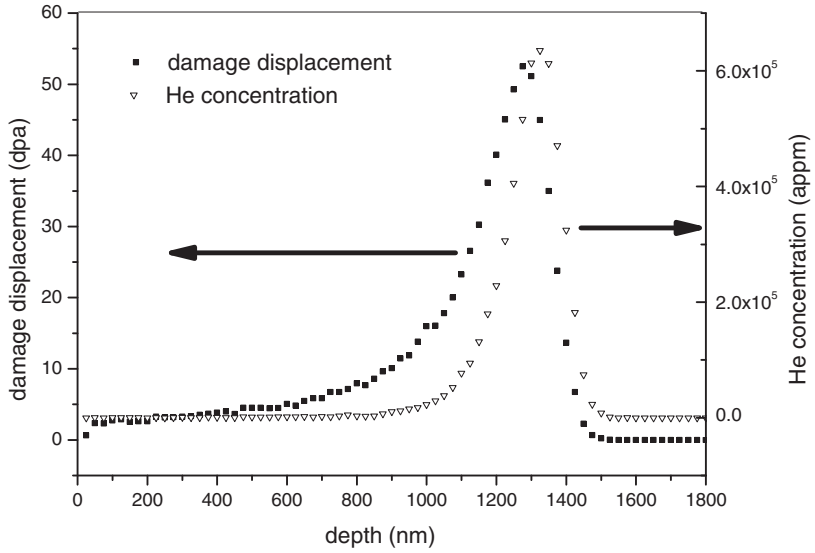


**Fig. 1.** He concentration and number of displacements per atom induced by 500 keV He irradiation at the dose of $1.0 \times 10^{18}$ ions $cm^{-2}$.

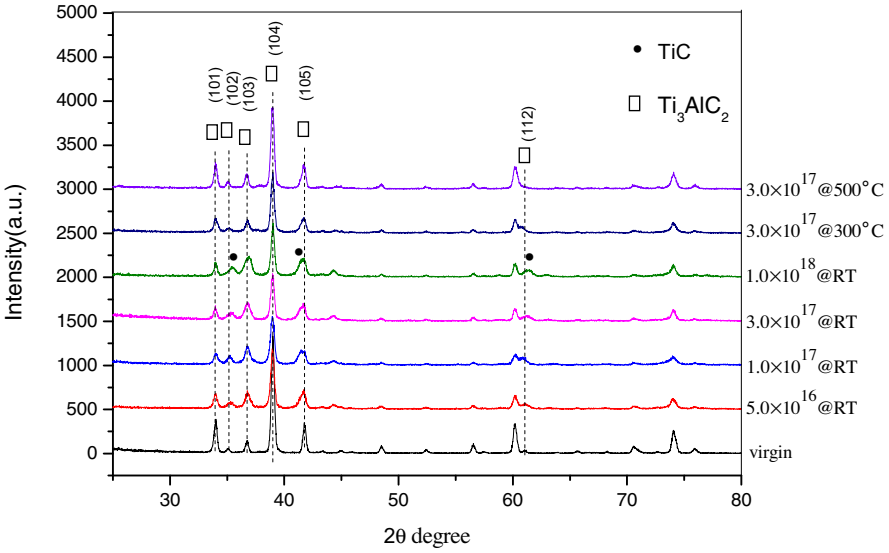


**Fig. 2.** XRD patterns of $Ti_3AlC_2$ samples irradiated at various doses and temperatures.



interstitial atoms or dislocation loops. And it becomes wider in the direction of helium implantation and more distinct owing to more defects when the dose increases. With the dose rising to $3.0 \times 10^{17}$ ions $cm^{-2}$, some bubbles grow bigger resulting in the average bubble radius of ~0.8 nm by means of absorbing the injected He atoms and vacancies from continuous irradiation damage. Meanwhile, some spherical bubbles appear to coalesce into strings, leading to a reduction in interfacial energy [17]. It is especially apparent at the maximum concentration depth of implanted helium (see Fig. 3c). In addition, the orientation of string-like bubbles along the direction parallel to the surface irrespective of the crystallographic orientation of the polycrystalline grains can minimize their system free energy. The same case happens in other ceramics such as $MgAl_2O_4$, $Al_2O_3$ and SiC with He ions irradiation at room temperature [18]. As the dose reaches $1.0 \times 10^{18}$ ions $cm^{-2}$, the coalescence of bubbles tend to be more pronounced with small cracks appearing (circles in Fig. 3d). The cracks are within ~50 nm in length. Additionally, Ofan's experiments [17] confirmed that the bubble size and the average distance between bubbles exerted crucial influence on the formation of the string-shaped bubbles. When the average distance between bubbles is on the order of the bubble size, the bubbles interact strongly, coalescing into string. However, in the current work no large cracks are observed under this irradiation condition.

As the irradiation temperature increases, the damaged region becomes narrower, and the boundary between the irradiated area and the virgin material is less visible along with the weak contrast in TEM images as shown in Fig. 4. They should be ascribed to fewer remaining defects caused by the increasing probability of recombination of Frenkel pairs at high temperatures. It is noticeable that the small cracks induced by bubbles coalescence disappear in Fig. 4b, but the mean bubble radius (~0.80 nm) remained constant (Fig. 4a). It indicates that the lower bubble concentration for the maximum peak depth is at the irradiation temperature of 300 °C. With increasing temperature, the removal rate increases faster than helium absorption [19]. So helium bubbles disperse into a larger zone. However, the temperature of 300 °C is not high enough for bubbles to grow eminently in $Ti_3AlC_2$. In Fig. 4c, the platelet-like, string- and sphere-shaped bubbles in different sizes are distributed regularly with implantation depth. The distribution is closely related to the varying concentration of deposited He atoms with increasing depth. In zone I of the damaged area, the spherical bubbles, generally more than 2 nm in diameter, exist for the major portion and a few string-shaped bubbles of up to 10 nm in length appear when the depth increases. In zone II, large platelet-like bubbles are oriented nearly in the direction of the multilayered structure with scattered spherical and string-shaped bubbles around them. Moreover, the orientation is not actually parallel to the irradiated surface but dependent on the specific crystallographic orientation of the polycrystalline grains to a certain extent. Although the orientations of platelet-like bubbles and the crystallographic orientation are not identified in the present study, the last phenomenon can be directly observed in some related high magnification TEM pictures (not presented here). So it is likely that platelet-like bubbles formation tends to be preferentially associated with the multilayered structure. Besides, the growth of bubbles should be explained by the Ostwald ripening process and void agglomeration [20–22].

### 3.3. Evolution of micro-srain

Generally, the X-ray diffraction peak broadening consists of the instrumental broadening and the broadening which is due to crystallite size and micro-strain present in the material. According to Liu and Nappé's analysis [8,15], the crystallite size of more than 1 μm (about 1.5 μm in this work) is large enough not to induce the broadening of the $Ti_3AlC_2$ diffraction peaks. So the Williamson–Hall (W–H) equation [23] for the peak broadening induced by micro-strain is given below:

$$(\beta_{hkl})^s = 4\,\varepsilon \tan\theta_{hkl} \qquad (1)$$

where $\theta_{hkl}$ is Bragg diffraction angle (°), $\varepsilon$ is the micro-strain and the experimental value of $(\beta_{hkl})^s$ is obtained following by eliminating the instrumental broadening. The analysis is carried out on the basis of the strong peaks of (101), (103), (104), (105), (110). And the micro-strain as the functions of dose and temperature is delineated in Fig. 5.

The irradiations at RT lead to a continuous increase in the micro-strain as the dose rises to $3.0 \times 10^{17}$ ions $cm^{-2}$, which is attributed to the more produced Frenkel pairs in materials. However, when the dose increases unceasingly, the micro-strain begins to decline due to the thermal effect [24,25]. With the identical irradiation dose (e.g., $3.0 \times 10^{17}$ ions $cm^{-2}$), the higher temperature, the lower the micro-strain. It verifies that temperature plays a crucial role in releasing the micro-stress.

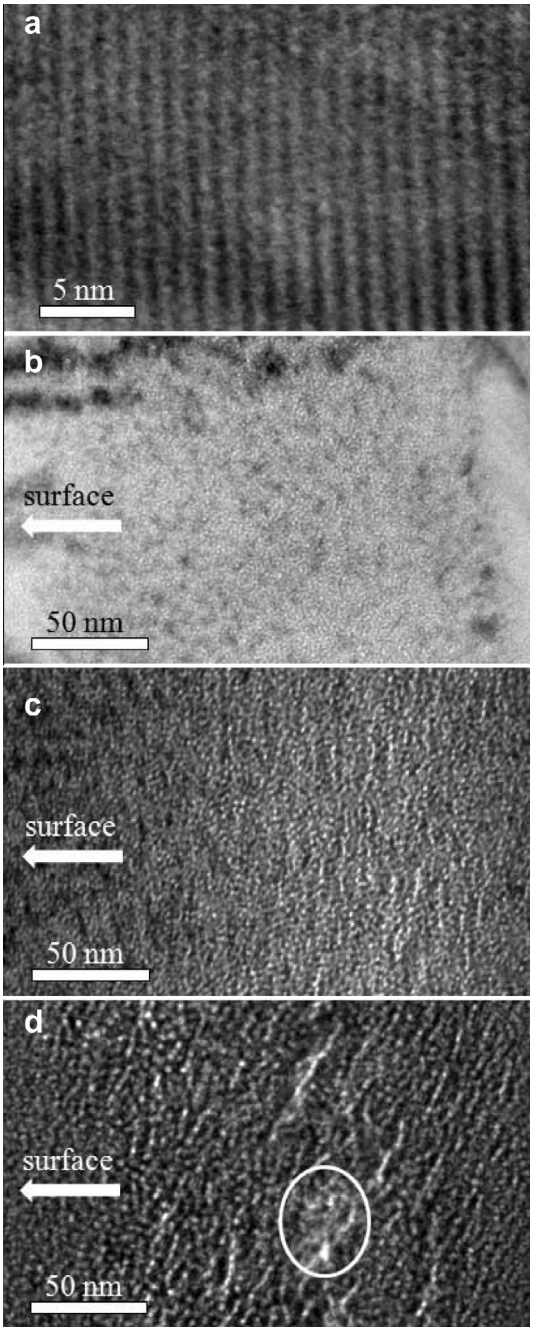


**Fig. 3.** (a) The bright-field TEM image of the virgin $Ti_3AlC_2$ and (b) to (d) corresponding to the samples irradiated at RT with doses of $5.0 \times 10^{16}$ ions $cm^{-2}$, $3.0 \times 10^{17}$ ions $cm^{-2}$, $1.0 \times 10^{18}$ ions $cm^{-2}$, respectively.

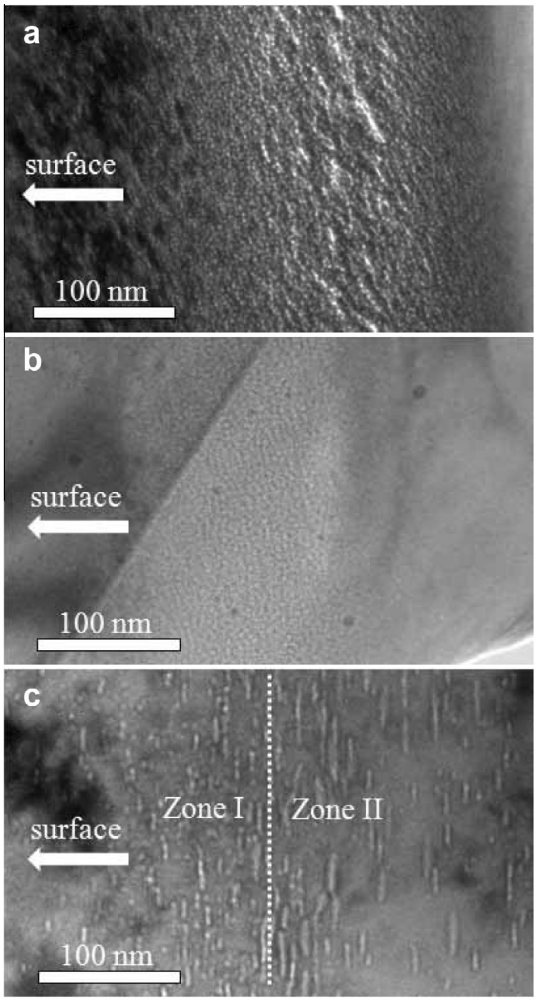


**Fig. 4.** (a)–(c) Corresponding the cross-section bright-field TEM images of $Ti_3AlC_2$ samples irradiated with the dose of $3.0 \times 10^{17}$ ions $cm^{-2}$ at RT, 300 °C, 500 °C, respectively.

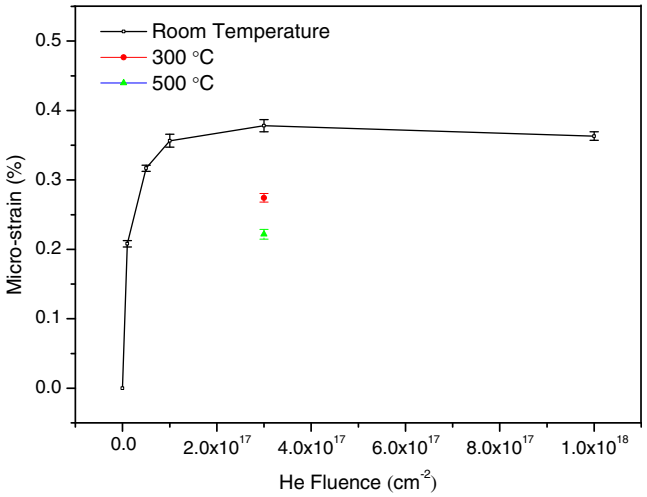


**Fig. 5.** Variation of the micro-strain derived from XRD results as a function of irradiation dose and temperature.

## 4. Discussion

Helium atoms in irradiated materials may exist in two forms: (i) helium-vacancy complexes for the low concentration of implanted helium atoms and (ii) helium bubbles or voids for the high concentration. Both may play a deleterious role for the structural properties [10,26] and physical properties of materials [27]. However, $Ti_3AlC_2$ shows irradiation resistance and recovery when irradiated by 500 keV helium ions under different conditions.

Similar to $Ti_3SiC_2$ [15], $Ti_3AlC_2$ is sensitive to elastic collisions rather than electronic excitation (inelastic collisions). So many vacancies and self-interstitials are created in the collision cascade with 500 keV He ions irradiation. Al atoms can easily escape from its position due to the weak bonding between Ti and Al [28]. Moreover, the theoretical calculations on helium incorporation in $Ti_3AlC_2$ demonstrate that helium atoms favor the interstitial and

substitutional sites in aluminum layer [29]. As a product of the decomposition of $Ti_3AlC_2$, the new phase TiC is formed even at the lowest damage level (2.6 dpa). But TiC almost disappears at the irradiation temperature of 500 °C, in coincidence with the phenomenon that the interstitial Si atoms could easily hop back to low energy 2*b* original site in $Ti_3SiC_2$ at high temperature (300, 500 °C) [8]. It is noteworthy that the occupation of Al sites by helium atoms does not influence the structural recovery of $Ti_3AlC_2$. Besides, $Ti_3AlC_2$ remains crystalline even at the maximum helium concentration of $\sim 6.4 \times 10^5$ appm and the corresponding damage level of $\sim$52 dpa ($1.0 \times 10^{18}$ ions $cm^{-2}$). Unlike it, SiC becomes amorphous above 0.5 dpa [30]. The direct reason for SiC going into the amorphous state should be due to the deposited energy produced by injected ions [27]. However, for $Ti_3AlC_2$, high resistance to amorphization should be attributed to the recovery from damage on basis of the diversity chemical bonds especially its strongest bond Ti–C [31].

Another important phenomenon is that no large cracks are observed at the highest fluence ($1.0 \times 10^{18}$ ions $cm^{-2}$), this is a discrepancy as compared with the result in Wang et al. [11]. The cause of the discrepancy should be the significant thermal effect on the He ions irradiation. The thermal effect becomes more significant as the irradiation dose reaches $1.0 \times 10^{18}$ ions $cm^{-2}$, which can be reflected by the tendency of micro-strain versus dose. And the sudden decline of micro-strain under this condition may be closely linked to the disappearance of large cracks. Besides, when the irradiation temperature rises up to 500 °C, the concentration of defects and the micro-strain see a consistent declining tendency. Moreover, the bubbles remain in small size due to their limited growth relevant to the nanolamellar structure of $Ti_3AlC_2$. Platelet-like bubbles form as a result of the anisotropic growth. The above outcomes demonstrate that $Ti_3AlC_2$ can stand the helium ions irradiation even at high temperature (500 °C).

## 5. Conclusion

The aim of this study was to evaluate the irradiation resistance of $Ti_3AlC_2$ with 500 keV He ion irradiation. $Ti_3AlC_2$ exhibits excellent resistance against He ion irradiation. When the damage level increases up to 52.2 dpa with the room temperature irradiations, neither amorphization happens nor large cracks appear. And the micro-stress in $Ti_3AlC_2$ gets released evidently at the highest dose. For the samples irradiated with the dose of $3.0 \times 10^{17}$ ions $cm^{-2}$, the produced new phase TiC disappears gradually, and the crystal structure (e.g., unit cell parameter) recovers significantly with increasing irradiation temperature. Moreover, at the temperature of 500 °C, helium bubbles don't agglomerate apparently because their growth is constrained by the nanolamellar structure of $Ti_3AlC_2$.



## Acknowledgments

This research project was supported by the Major State Basic Research Development Program of China ('973' Program, Grant No. 2010CB832902) and the National Natural Science Foundation of China (NSFC) (Grant Nos. 91126011, 11275005 and 11275238).

## References

[1] M.W. Barsoum, M. Radovic, Annu. Rev. Mater. Res. 41 (2011) 195.
[2] M.W. Barsoum, H.I. Yoo, I.K. Polushina, V.Yu. Rud, Yu.V. Rud, T. El-Raghy, Phys. Rev. B 62 (2000) 10194.
[3] E.H. Kisi, J.A.A. Crossley, S. Myhra, M.W. Barsoum, J. Phys. Chem. Solids 59 (1998) 1437.
[4] X.H. Wang, Y.C. Zhou, Chem. Mater. 15 (2003) 3716.
[5] M.L. Flem, X. Liu, S. Doriot, T. Cozzika, I. Monnet, Int. J. Appl. Ceram. Technol. 7 (2010) 766.
[6] K.R. Whittle, M.G. Blackford, R.D. Aughterson, S. Moricca, G.R. Lumpkin, N.J. Zaluzec, Acta Mater. 58 (2010) 4362.
[7] X.M. Liu, M.L. Flem, J.L. Béchade, I. Monnet, J. Nucl. Mater. 401 (2010) 149.
[8] X. Liu, M.L. Flem, J.L. Béchade, F. Onimus, T. Cozzika, I. Monnet, Nucl. Instrum. Methods B 268 (2010) 506.
[9] R.E. Stoller, J. Nucl. Mater. 174 (1990) 289.
[10] H. Ullmaier, Radiat. Eff. 78 (1983) 1.
[11] C. Wang, T. Yang, S. Kong, J. Xiao, J. Xue, Q. Wang, C. Hu, Q. Huang, Y. Wang, J. Nucl. Mater. 440 (2013) 606.
[12] www.srim.org.
[13] C. Liu, L. Shi, Q. Qi, D.J. O'Connor, B.V. King, E.H. Kisi, X.B. Qing, B.Y. Wang, Nucl. Instrum. Methods B 307 (2013) 536.
[14] L. Zhang, Q. Qi, L.Q. Shi, D.J. O'Connor, B.V. King, E.H. Kisi, D.K. Venkatachalam, Appl. Surf. Sci. 258 (2012) 6281.
[15] J.C. Nappé, I. Monnet, Ph. Grosseau, F. Audubert, B. Guilhot, M. Beauvy, M. Benabdesselam, L. Thomé, J. Nucl. Mater. 409 (2011) 53.
[16] L. Farber, I. Levin, M.W. Barsoum, T. El-Raghy, T. Tzenov, J. Appl. Phys. 86 (1999) 2540.
[17] A. Ofan, L. Zhang, O. Gaathon, S. Bakhru, H. Bakhru, Y. Zhu, D. Welch, R.M. Osgood, Phys. Rev. B 82 (2010) 104113.
[18] S.J. Zinkle, Nucl. Instrum. Methods B 286 (2012) 4.
[19] J. Chen, P. Jung, H. Trinkaus, Phys. Rev. Lett. 82 (1999) 2709.
[20] W. Hua, S.D. Yao, N.D. Theodore, M. Martin, A. Aitkaliyeva, L. Shao, Radiat. Eff. Defects Solids 165 (2010) 388.
[21] G.W. Greenwood, A. Boltax, J. Nucl. Mater. 5 (1962) 234.
[22] H. Trinkaus, B.N. Singh, J. Nucl. Mater. 323 (2003) 229.
[23] G.K. Williamson, W.H. Hall, Acta Metall. 1 (1953) 22.
[24] J.R. Sun, Z.G. Wang, Y.Y. Wang, C.F. Yao, K.F. Wei, F.S. Li, Nucl. Instrum. Methods B 269 (2011) 873.
[25] J.R. Sun, Z.G. Wang, Y.Y. Wang, Y.B. Zhu, L.L. Pang, T.L. Shen, F.S. Li, Nucl. Instrum. Methods B 286 (2012) 277.
[26] G. Velisa, A. Debelle, L. Vincent, L. Thomé, A. Declémy, D. Pantelica, J. Nucl. Mater. 402 (2010) 87.
[27] C. Tromas, V. Audurier, S. Leclerc, J. Nucl. Mater. 373 (2008) 142.
[28] H.Z. Zhang, S.Q. Wang, Acta Mater. 55 (2007) 4645.
[29] J. Xiao, C. Wang, T. Yang, T. Yang, S. Kong, J. Xue, Y. Wang, Nucl. Instrum. Methods B 304 (2013) 27.
[30] W.J. Weber, L.M. Wang, Nucl. Instrum. Methods B 106 (1995) 298.
[31] L.F. Marion, I. Monnet, J. Nucl. Mater. 433 (2012) 534.